ELSEVIER
Available online at www.sciencedirect.com
SCIENCE DIRECT®
Journal of Catalysis 235 (2005) 251–261
JOURNAL OF CATALYSIS
www.elsevier.com/locate/jcat

The effect of Ni in Pd–Ni/(Ce,Zr)O_x/Al_2O_3 catalysts used for stoichiometric CO and NO elimination. Part 1: Nanoscopic characterization of the catalysts

A.B. Hungría [a,*], N.D. Browning [b,c], R.P. Erni [b,c], M. Fernández-García [a], J.C. Conesa [a], J.A. Pérez-Omil [d], A. Martínez-Arias [a,*]

[a] *Instituto de Catálisis y Petroleoquímica, CSIC, C/ Marie Curie 2, Campus Cantoblanco, 28049 Madrid, Spain*
[b] *National Center for Electron Microscopy, LBNL, Berkeley, CA 94720, USA*
[c] *Department of Chemical Engineering and Materials Science, University of California-Davis, Davis, CA 94720, USA*
[d] *Dpto. de Ciencia de los Materiales e Ingeniería Metalúrgica y Química Inorgánica, Facultad de Ciencias, Universidad de Cádiz, 11510 Puerto Real, Cádiz, Spain*

Received 18 March 2005; revised 6 July 2005; accepted 16 August 2005

Abstract

Pd–Ni catalysts supported on Al_2O_3, (Ce,Zr)O_x/Al_2O_3, and (Ce,Zr)O_x are characterized at a nanoscopic level using mainly electron microscopy-related techniques (HREM images, XEDS, and Z-contrast images/EELS spectra done with TEM and STEM instruments). The presence of rather homogeneous Ce–Zr mixed oxide nanostructures is revealed from analysis of HREM pictures. Analysis of the Pd–Ni/(Ce,Zr)O_x/Al_2O_3 system shows the existence of preferential interactions of Pd and Ni with the (Ce,Zr)O_x and Al_2O_3 components, respectively, as evidenced mainly by XEDS and confirmed by FMR. Dispersion states of the metals and particle size distributions of palladium are inferred from analysis of Z-contrast images and EELS spectra. The results are complemented by XPS and XAFS results used to analyse the chemical state of the metallic components in the catalysts and their dispersion over the different supports.

Keywords: Pd–Ni catalysts; CeO_2–ZrO_2; Al_2O_3; HREM; XEDS; STEM-EELS; Z-contrast images; FMR; XANES; XPS

1. Introduction

Three-way catalysts (TWCs) are widely used to diminish pollutant emissions from gasoline engine-powered vehicles [1]. Classical components of these systems usually include Rh, Pt, and/or Pd as active metals; ceria as promoter; and high-surface area alumina as the support [1,2]. In modern TWC formulations, the classical promotion by ceria has been extended to other structurally related oxide systems to increase or maintain the durability of the TWC while enhancing oxygen storage capacity (OSC) properties of the catalyst [2,3]. In this sense, Ce–Zr mixed oxide systems, and particularly in alumina-supported Ce–Zr mixed-oxide configurations, have been considered as optimum metal supports on the basis of their greater oxygen storage capacity (OSC) after thermal sintering, which could potentially increase the useful lifetime of the catalytic system [3].

Concerning the active metal, the use of Pd as the only active metal component in TWC has received considerable attention on the basis of economic factors (i.e., the high cost and scarcity of Rh), the availability of cleaner fuels, and its remarkable activity for hydrocarbon and CO oxidation reactions [1,2,4]. Nevertheless, the increasingly stricter limits imposed worldwide for automobile toxic emissions have forced consideration of new aspects and requirements in TWCs. Among these, the achievement of lower light-off temperature during the cold start phase is of the greatest relevance, considering that the largest portion of the toxic emissions is produced during that period [1]. An interesting approach in this sense involves promoting Pd with lower-cost base metals [2]. Promising results in this respect have been obtained by using Mn, Cr, or Cu, which have been attributed to the formation of the corresponding alloys (with consequent perturbation of the Pd electronic properties) or, in

---

[*] Corresponding authors.
E-mail addresses: abhungria@icp.csic.es (A.B. Hungría), amartinez@icp.csic.es (A. Martínez-Arias).

0021-9517/$ – see front matter © 2005 Elsevier Inc. All rights reserved.
doi:10.1016/j.jcat.2005.08.011

the case of Mn, to a mixture of effects involving alloy formation and Pd–MnO_x interactions [5–8]. Another metal that may be considered as a potential promoter of Pd activity for these reactions (despite legislative restrictions on its use in some nations) is Ni. Thus, recent reports by researchers at Nissan (Japan) have shown the beneficial effect of establishing contacts between Pd and Ni, particularly for enhancing NO_x conversion activities under stoichiometric or rich atmospheres [9]. This has been mainly attributed to operation through a bifunctional mechanism by which nickel (basically in the form of nickel aluminate) provides sites for NO adsorption and subsequent transfer to the active Pd sites.

In the aforementioned context, the present work examines the catalytic properties of Pd–Ni systems for reactions of interest in the TWC field, such as CO oxidation and NO reduction. This first part of the work is dedicated to determining the structural/morphological characteristics of the different components of the catalysts, as well as identifying possible associations between them, taking into account the particular relevance of these aspects to explain the catalytic behavior of the systems [8,10–12]. To achieve this goal, a multitechnique approach (X-ray diffraction [XRD], high-resolution electron microscopy [HREM], STEM–X-ray dispersive spectroscopy [XEDS], ferromagnetic resonance [FMR], XAFS, and X-ray photoelectron spectra [XPS]) was used to characterize the catalysts supported on Al_2O_3, $(Ce,Zr)O_x$, or $(Ce,Zr)O_x/Al_2O_3$. Particular attention was given to the catalyst supported on the latter, which is probably the most interesting from a practical standpoint, taking into account the generally lower thermally induced deactivations achieved over such types of complex supports in comparison with the individual oxide components [3,13–15]. Characterization results obtained in this first part of the work are correlated with catalytic properties in the second part [12].

2. Experimental

Pure alumina (γ-Al_2O_3, Condea Puralox), ceria–zirconia/alumina with 10 wt% of Ce–Zr mixed oxide content (expressed, in accordance with ICP-AES analysis, as $Ce_{0.5}Zr_{0.5}O_2$), and a Ce–Zr mixed-oxide material (the composition of which, according to ICP-AES analysis, is close to $Ce_{0.5}Zr_{0.5}O_2$) were used as supports (these are referred to hereinafter as A, CZA, and CZ, respectively). CZA and CZ were prepared by equimolar cerium–zirconium coprecipitation within reverse microemulsions followed by separation of the solid, rinsing with methanol, drying overnight at 393 K, and calcination under air at 773 K for 2 h. S_{BET} values of 196, 195, and 132 $m^2\,g^{-1}$ were obtained for A, CZA, and CZ, respectively. Full details of the procedure and materials used in these microemulsion preparations have been reported elsewhere [8,16]. The supports were coimpregnated (using the incipient wetness method) with aqueous solutions of Pd(II) and Ni(II) nitrates (to achieve 1 wt% loadings for each of the metals in the final catalysts), followed by overnight drying at 393 K and calcination under air at 773 K for 2 h. Supported monometallic Pd or Ni reference catalysts (with 1 wt% loading in any case) were prepared by the same method. No appreciable differences in S_{BET} values with respect to those of the supports were observed on incorporation of the metals. Bulk NiO (from Alfa Aesar) and $NiAl_2O_4$ (prepared by calcination of a mixture of nickel and aluminum nitrates under air at 1473 K, as reported elsewhere [17]) were used as references, with their purity confirmed by XRD.

XRD patterns were recorded on a Seifert diffractometer using nickel-filtered Cu-K_α radiation, operating at 40 kV and 40 mA, with a 0.02° step size and a counting time of 5 s. HREM images were recorded using a JEOL 2000 EX microscope, equipped with a top-entry specimen holder, with 0.21-nm point-to-point resolution. The experimental micrographs were digitized using a CCD camera (COHU-4910). Digital image processing was performed using the SEMPER 6+ software. Some of the samples were also examined by transmission electron microscopy (TEM) using a Philips CM200 FEG with 0.24-nm point-to-point resolution, incorporating XEDS analysis, for which it was equipped with a EDAX DX4 detector. The sample spot for XEDS analysis was at least 20 nm. XEDS analysis in nanoprobe mode (beam size of ca. 2 nm) was performed with another Philips CM200 FEG microscope equipped with a Link Energy dispersive X-ray detector.

Z-Contrast imaging and EELS were performed in a 200-kV F20 UT Tecnai microscope operating in STEM mode. The STEM spatial resolution was 0.14 nm, and the EELS energy resolution was 0.5 eV.

For the HREM, TEM-XEDS, and STEM experiments, portions of the sample were crushed in an agate mortar and suspended in hexane. After ultrasonic dispersion, a droplet was deposited on a copper grid supporting a perforated carbon film.

FMR spectra were recorded with a Bruker spectrometer (ER 200D) working in the X-band and calibrated with a DPPH standard. Spectra presented in this work were recorded at 77 K for samples reduced under 100 Torr of H_2 at 773 K for 30 min, followed by outgassing at the same temperature for 15 min.

XPS were acquired with a VG ESCALAB 200R spectrometer equipped with a hemispherical electron analyzer and an Al-K_α 120 W X-ray source. The powder samples were pressed into small aluminum cylinders, then mounted on a sample rod placed in an in situ pretreatment chamber and treated thoroughly under vacuum at room temperature and then at 473 K for 1 h, followed by treatment under O_2 at 473 K before being moved into the analysis chamber adjacent to the pretreatment chamber. The pressure in the ion-pumped analysis chamber was maintained below 3×10^{-9} Torr ($1\ \text{Torr} = 133.33\ \text{N}\,\text{m}^{-2}$) during data acquisition. The intensities were estimated by calculating the integral of each peak (or a set of them) after subtracting a "S-shaped" Shirley-type background and using experimental sensitivity factors from the literature [18]. The C1s peak from adventitious adsorbed species could not be used to reference binding energies (BEs), because it gave incoherent results, indicating the varying nature of these species in the different samples. Instead, the Al2p peak, taken to occur at 74.0 eV, was used for the alumina-containing specimens, whereas for those supported on CZ the u''' peak of the Ce3d spectrum, characteristic of Ce^{4+}, was taken to occur at 916.8 eV, as observed in pure ceria [19]. (The use of this value is consistent with the average of values obtained for the other samples examined; furthermore, as verified by principal component analysis, it normally does not change in response to redox changes or mixed-oxide formation [20].) BE values probably have uncertainties around 0.2 eV, whereas relative atomic ratios are determined with a precision of ±7%.

X-Ray absorption experiments at the Ni and Pd K-edges were performed on station 9.3 of the SRS Daresbury Laboratory synchrotron equipped with a Pd-coated plane mirror and a Si(220) double-crystal monochromator set at 50% harmonic rejection detuning. Transmission experiments were carried out using noble gas-filled ionization chambers. The energy scale was simultaneously calibrated by measuring a Ni or Pd foil using a third ionization chamber and giving a value of 8333 or 24,350 eV, respectively, to the first inflection point. Samples were self-supported (absorbance = 0.5–1.0) and placed in a controlled-atmosphere cell for in situ pretreatment under diluted oxygen flow at 773 K. After this treatment, XANES spectra were recorded at room temperature. EXAFS spectra were obtained at room temperature in the range −80 to 850 eV (from the edge position), accumulating for ca. 3 h.

3. Results and discussion

3.1. Characterization of the supports

Previous reports have analyzed the main characteristics of the supports used from the standpoint of bulk characteristics (based mainly on XRD, Raman, and conventional TEM-XEDS results [20,21]). Table 1 summarizes the main findings of such studies. Basically, the results revealed the presence of Ce–Zr mixed oxide structures displaying the tetragonal phase t″ (a fluorite-related "pseudocubic" phase, because it shows a lattice parameters ratio $c/a = 1$, with its diffraction peaks thus being indexed in the $Fm3m$ space group, whereas the overall tetragonal symmetry is due to distortion of the anionic sublattice [3,22,23]), which likely becomes stabilized as a consequence of its nanosized nature [23,24]. Surface characteristics of the Ce–Zr mixed oxide in CZA and CZ (on the basis of FTIR and EPR studies using probe molecules as well as XPS results) were also analyzed in previous works and were in accordance with the presence of mixed-oxide surface characteristics for these particles [20,25]. Besides this, in addition to Ce–Zr mixed-oxide particles (Table 1), O_2-probe EPR experiments revealed the presence of highly dispersed Ce–Zr mixed oxide entities in CZA undetectable by diffraction techniques (probably in the form of two-dimensional patches) [21,25,26].

Further insights into the structural properties of CZA and CZ supports, complementing the results of Table 1, are presented here on the basis of a HREM study. Multiple (about 50) high-resolution micrographs have been registered for each of these samples. These micrographs generally show the presence of multiple particles displaying interference fringes patterns. For CZA, such patterns appear only for zones with appreciable loadings of Ce–Zr mixed oxide and are not detected in zones richer in γ-Al_2O_3. Unfortunately, this disallows the determination of possible epitaxial relationships between γ-Al_2O_3 and Ce–Zr mixed-oxide particles. Fig. 1 shows micrographs representative for these samples along with digital diffraction patterns (DDPs) characteristic of the observed particles. The pictures show the presence of nanoparticles of the Ce–Zr mixed oxide for both samples, some of them well faceted. Interplanar spacings and angles observed in the DDP are compatible with the presence of a cubic fluorite or a tetragonal (pseudocubic) phase t″ of the Ce–Zr mixed oxide. Attempts to resolve differences between these two phases on the basis of the presence of specific extra spots (in particular, a kinetic extinction of type 001) in the patterns originating from the tetragonal phase were unsuccessful [15]. Nevertheless, the Raman spectrum of CZ allowed unambiguous identification of the crystalline phase in this sample as the tetragonal one t″ (Table 1). Such a phase can also be the one in which the Ce–Zr mixed-oxide particles in CZA crystallize. In fact, previous results on a sample of a similar type but with a higher mixed-oxide loading revealed the presence of such a phase with particle sizes relatively close (about 1.0–1.5 nm larger on average) than those observed for CZA [21]. Nevertheless, on the basis of the results obtained, stabilization of the cubic phase for the very small Ce–Zr mixed-oxide particles found in CZA, as has been reported for zirconia nanocrystals (smaller than ca. 2 nm) based on TEM experiments, cannot be discounted [23,27]. It also must be noted that possible effects in either sense (stabilization of the cubic or tetragonal phase of the Ce–Zr mixed oxide) of the interaction with the underlying alumina are difficult to resolve. Nanocrystal particle size distributions of the Ce–Zr mixed oxide, obtained from an analysis using Feret's diameters [28], are shown in Fig. 2. Average values obtained from this analysis are in fair agreement with those observed previously using other techniques (Table 1). In summary, these results reveal the presence

Table 1
Summary of XRD, TEM/XEDS and Raman results for the supports employed [20,21]

Support	Crystalline phases detected[a]	$(Ce,Zr)O_x$ particle size (nm)[b]	$(Ce,Zr)O_x$ cell parameter (Å)	Ce/Zr atomic ratio[c]
A	γ-Al_2O_3			
CZA	γ-Al_2O_3, $(Ce,Zr)O_x$ (c or t″)[d]	2–3	5.30	0.9–1.1
CZ	$(Ce,Zr)O_x$ (t″)	5.3	5.29	0.9–1.1

[a] X-Ray or electron diffraction and Raman results.

[b] From TEM dark-field images using the (111) ring of the fluorite-type structure (CZA) or bright-field images (CZ).

[c] XEDS results.

[d] X-Ray or electron diffraction patterns are compatible with both a cubic fluorite or a tetragonal t″ phase which is, in principle, indistinguishable by these techniques for the nanoparticles. The weakness of the bands in the Raman spectrum does not allow resolving this point.

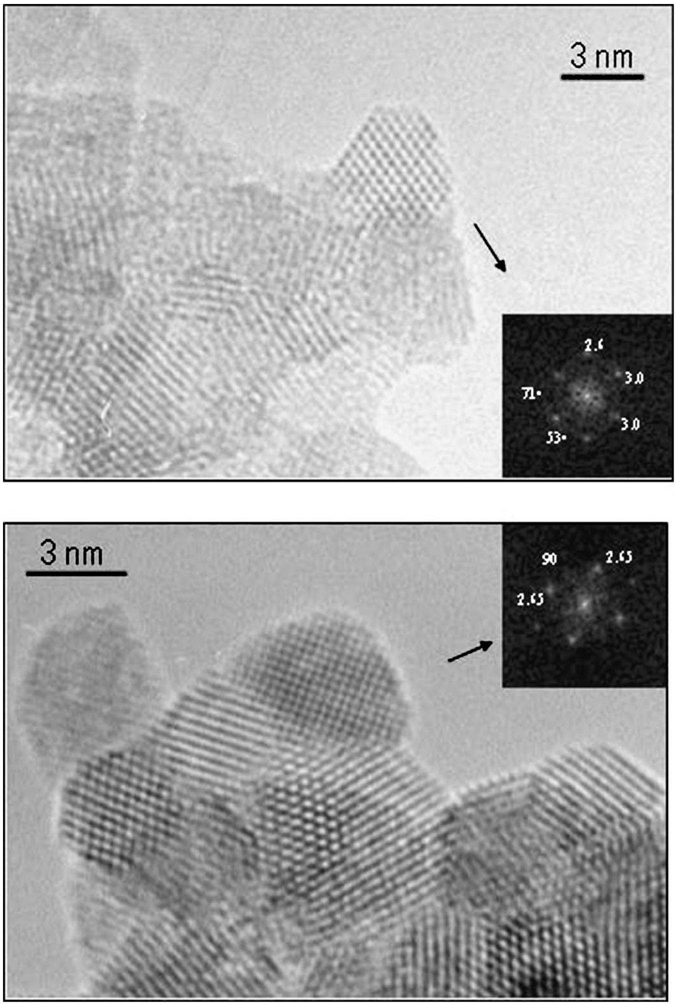

Fig. 1. HREM pictures representative of the CZA (top) and CZ (bottom) supports and digital diffraction patterns (as insets) typically observed for the corresponding Ce–Zr mixed oxide particles.

of nanosized configurations of the Ce–Zr mixed oxide in both CZ and CZA samples, with a larger particle size for the former and with fairly good compositional and morphological homogeneity (according to the XEDS results given in Table 1 and particle size distributions calculated in Fig. 2).

3.2. Characterization of the catalysts

No evidence of Ni or Pd particles was found on XRD, which displayed diffractions similar to those detected for the corresponding supports and identified as corresponding to γ-Al_2O_3 or Ce–Zr mixed-oxide phases [3,20,21], as detailed earlier. The nondetection of Pd- or Ni-containing phases suggests a relatively high dispersion of such components. Indeed, an HREM study of these catalysts revealed (in contrast to the observation of well-resolved Ce–Zr mixed-oxide particles similar to those described earlier for the supports) great difficulty identifying Pd- or Ni-containing particles in them, possibly due to the relatively high dispersion degree of these metals. In only a few cases could such particles be detected by HREM, and this occurred only for PdNiA or PdNiCZA and only on the basis of contrast differences, because no high-resolution fringes could be resolved for these. In contrast, no Pd- or Ni-related particles could be identified in the multiple pictures taken for PdNiCZ, suggesting a relatively higher dispersion state for the metal component in this system. These findings, along with the somewhat unstable character of these catalysts under the electron beam, preclude us from drawing conclusions based on this technique that can be taken as representative of the properties of the metal component in these catalysts.

To gain insight into the distribution of both metals over the support, as well as into possible associations between them or between any of the metals and either of the support components (most relevant to explain its catalytic properties [12]), the CZA-supported sample was thoroughly analyzed by XEDS.

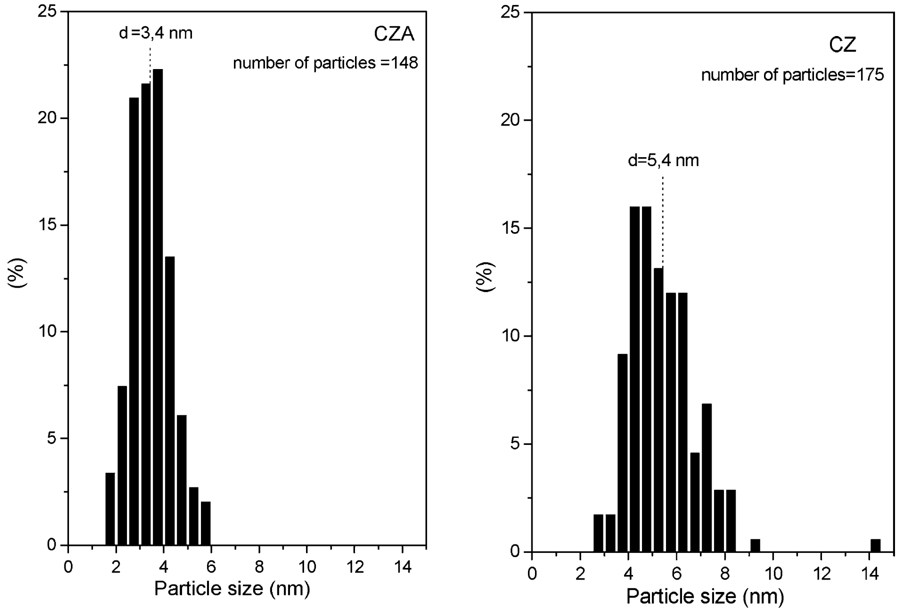

Fig. 2. Particle size distribution of the Ce–Zr mixed oxide particles extracted from HREM pictures of CZA (left) and CZ (right) supports. The vertical dashed line marks the average diameter ($d = \sum n_i d_i / \sum n_i$) obtained from the distribution.

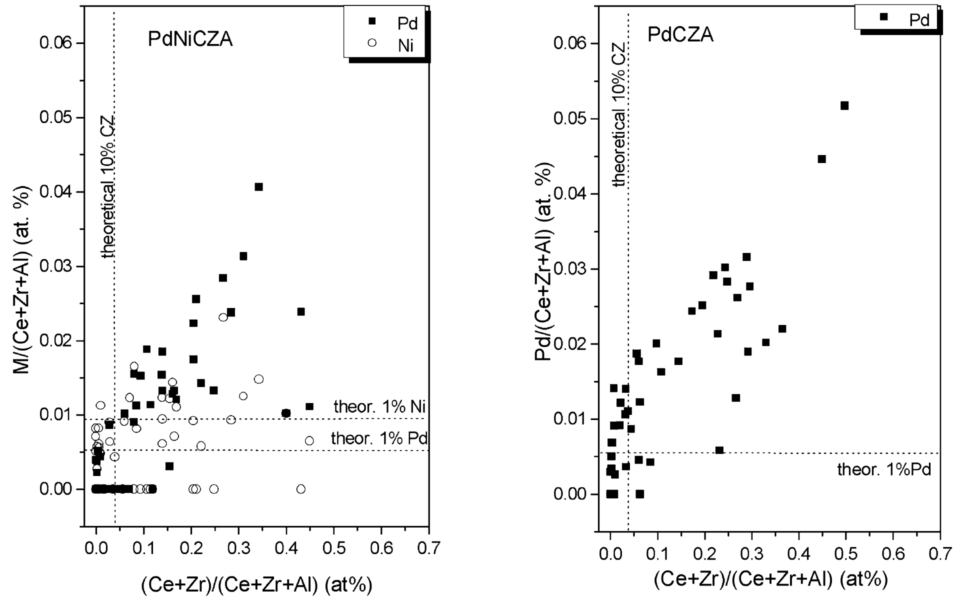

Fig. 3. XEDS results obtained from multiple analysis in different regions of the PdNiCZA (left) and PdCZA (right) catalysts using an electron beam of ca. 20 nm. Dotted lines mark theoretical positions according to chemical composition values.

Analysis at ca. 20 nm resolution revealed a clear trend of Pd to appear in zones enriched by Ce–Zr mixed oxide (hereinafter denoted by CZ) and Ni uniformly distributed throughout the entire compositional range (Fig. 3). Note that analysis of the more alumina-rich zones detected relatively lower amounts of Pd in the Pd–Ni catalyst, suggesting a preferential interaction between Pd and CZ in this system. To achieve a greater spatial resolution, a series of XEDS experiments were performed for PdNiCZA with a ca. 2-nm beam in the nanoprobe mode (see Experimental section). Fig. 4 shows the results of the multiple XEDS analyses performed in this mode. They unambiguously confirm the preferential association between Pd and CZ in this sample. In contrast, nickel appears to be preferentially associated with the alumina component of the catalyst.

To further explore this latter aspect, and considering that XEDS results obtained with a lower spatial resolution suggested a nickel distribution that was fairly homogeneous and independent on the support composition at a local level (Fig. 3), the samples were analyzed by FMR spectroscopy. This technique can provide information on small ferromagnetic or superparamagnetic metallic Ni particles [29]. For this purpose, the samples were reduced under hydrogen, to take advantage of the expected different reduction behaviors depending on whether nickel entities preferentially interacted with the alumina or with CZ [30,31]. Interactions between palladium and nickel can be also of relevance in this respect. Fig. 5 shows the spectra obtained for the different samples. The signals observed are quite broad and show varying levels of anisotropy, typical of small, reduced nickel particles [29]. Qualitative estimation of their intensity clearly shows a greater intensity for the nickel entities necessarily in contact with CZ (samples PdNiCZ and NiCZ). In contrast, the spectra of samples in which the nickel entities are in contact with alumina (samples PdNiA and NiA) exhibit a very low intensity. These results are in line with previous reports showing (mainly on the basis of TPR results) a greater facility for nickel reduction when using cerium-containing oxide supports rather than more inert ones like alumina [30,31]. On this basis, the relatively low intensity of the signals due to

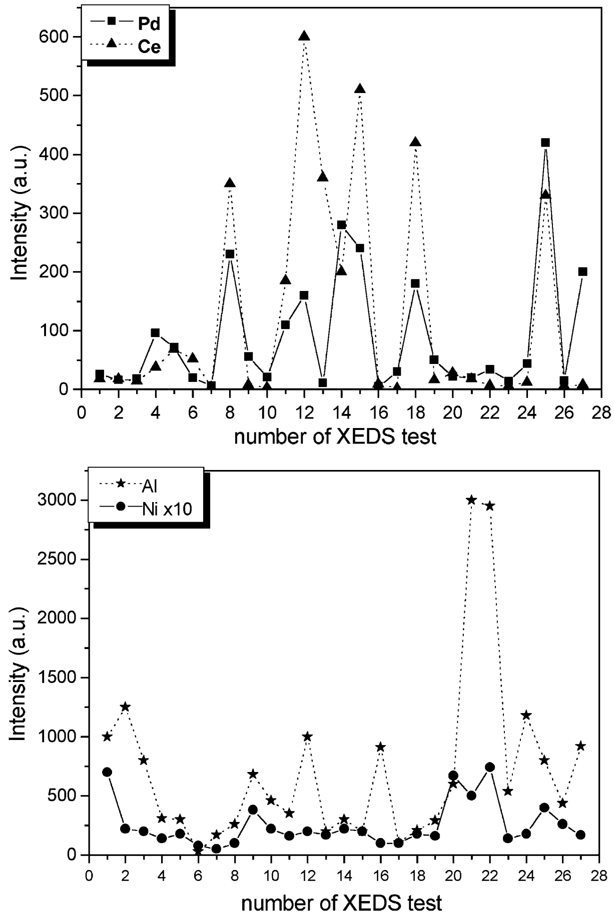

Fig. 4. XEDS results obtained from 27 tests performed in the nanoprobe mode of the PdNiCZA catalyst.

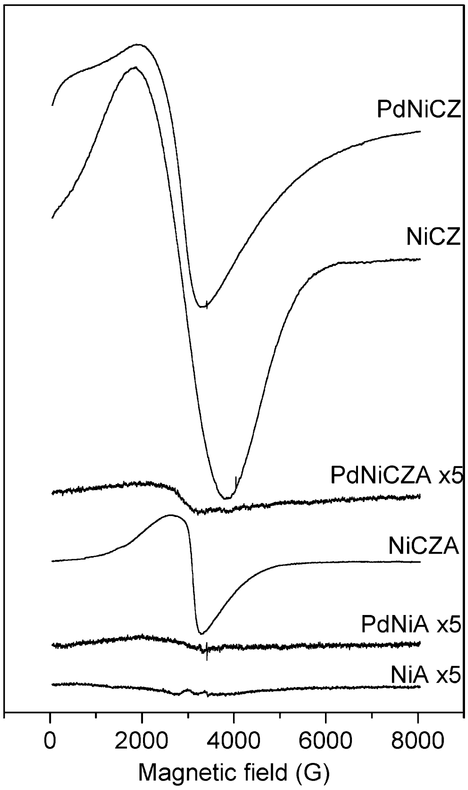

Fig. 5. Ferromagnetic resonance spectra recorded at 77 K of the indicated samples reduced under H_2 at 773 K.

small nickel particles observed for PdNiCZA strongly indicates that in this catalyst, most of the nickel is in contact with the alumina component of that catalyst, corroborating the XEDS results of Fig. 4. Differences between this latter and the NiCZA reference system, which shows a relatively higher intensity of reduced nickel entities, suggests that palladium presence favors a preferential interaction of nickel with the alumina component. Note that this latter finding is not likely due to differences in pH of the impregnating solutions used during catalyst preparation, because no significant pH difference was observed as a function of the presence of nickel in the solutions.

The higher stability toward reduction of nickel entities interacting with the alumina may be related to their stabilization in the form of a spinel aluminate like $NiAl_2O_4$. Because, according to previous reports [9,32], the presence of the latter can be relevant from the standpoint of the catalytic activity for reactions of CO and NO elimination, as analyzed in part 2 of this work [12], XPS and XANES spectroscopy were performed to gain insight into the nature of nickel entities in these catalysts. Table 2 collects data extracted from the XPS spectra of the Pd–Ni systems along with those obtained for the $NiAl_2O_4$ reference. The atomic ratio values estimated for the Pd–Ni catalysts are compatible with the presence of highly dispersed states for the nickel component, particularly for the CZ-supported system. Of note, lower nickel dispersion is apparent for PdNiCZA, which may be related to the tendency of this component to concentrate in alumina-enriched zones of the catalyst, in accordance with XEDS results (Fig. 4). In all samples examined, spectra in the $Ni2p_{3/2}$ binding energy region were composed of a main peak and a satellite peak at ca. 6 eV above the main peak, which represented about 40% of the whole $Ni2p_{3/2}$ intensity. The position of the main $Ni2p_{3/2}$ peak (Table 2) was compatible with a divalent state of nickel (as was further confirmed by XANES) in all cases. However, although the peak position observed for PdNiCZ appeared closer to that usually observed for NiO [33], the higher binding energy (E_B) observed for PdNiA and PdNiCZA suggests that nickel may form part of a nickel aluminate in these samples [34], also in agreement with results observed for the $NiAl_2O_4$ reference (Table 2). (The possibility that the relatively low E_B value displayed by PdNiCZ may be related to the existence of any type of interaction between Pd and Ni in this catalyst cannot be completely discounted, particularly considering that a NiCZ reference catalyst showed a somewhat higher $Ni2p_{3/2}$ E_B of 855.6 eV.) Nonetheless, it must be noted that such slightly higher E_B values have also been reported in nickel oxide samples (in both +2 and +3 valence states of nickel) [33–35].

Table 2
Summary of the XPS results

Sample	$Ni2p_{3/2}$ main peak E_B (eV)	Ni/(Ce + Zr + Al) atomic ratio
$NiAl_2O_4$	855.8	0.31
PdNiA	856.2	0.017
PdNiCZA	856.3	0.012
PdNiCZ	854.9	0.029

In an attempt to resolve these uncertainties, A- and CZA-supported samples were analyzed by XANES. Fig. 6 shows the XANES spectra of the NiA, PdNiA, and PdNiCZA samples and NiO and $NiAl_2O_4$ reference systems. Differences among the samples are minimal, indicating the similar nature of the Ni chemical state and distribution in these three bimetallic samples supported on alumina. The bottom of Fig. 6 shows the derivative spectra of one illustrative sample and the two reference compounds. The sample spectrum could be interpreted as a sum of NiO and $NiAl_2O_4$ contributions; significant intensity at the beginning of the edge (8335–8345 eV) indicates the presence of small NiO-type aggregates, whereas a clear match with the $NiAl_2O_4$ profile is visible at the end of the edge. Differences between the sample and the Ni-containing reference XANES spectra may be due to the small size of the Ni-containing oxide nanoparticles and the corresponding influence of their inherent disordered structure in XANES shape [23], eliminating the possibility of obtaining an estimation of the reference compound weights in each sample using a least squares fitting procedure. Taking this into account, it would seem that both Ni(II) chemical compounds could be present in similar proportions for these alumina-supported samples.

Given the difficulty in obtaining information on the characteristics of Pd- and/or Ni-containing particles by HREM, the catalysts were studied with an advanced microscope operating in STEM mode. In principle, this can allow the characterization of particle size, morphology, and valence state of such entities through simultaneous recording of Z-contrast images (with HAADF detection) and high spatial and energy resolution EELS spectra [36]. It must be noted that for the catalysts studied in this work, identification or localization of the Pd- and/or

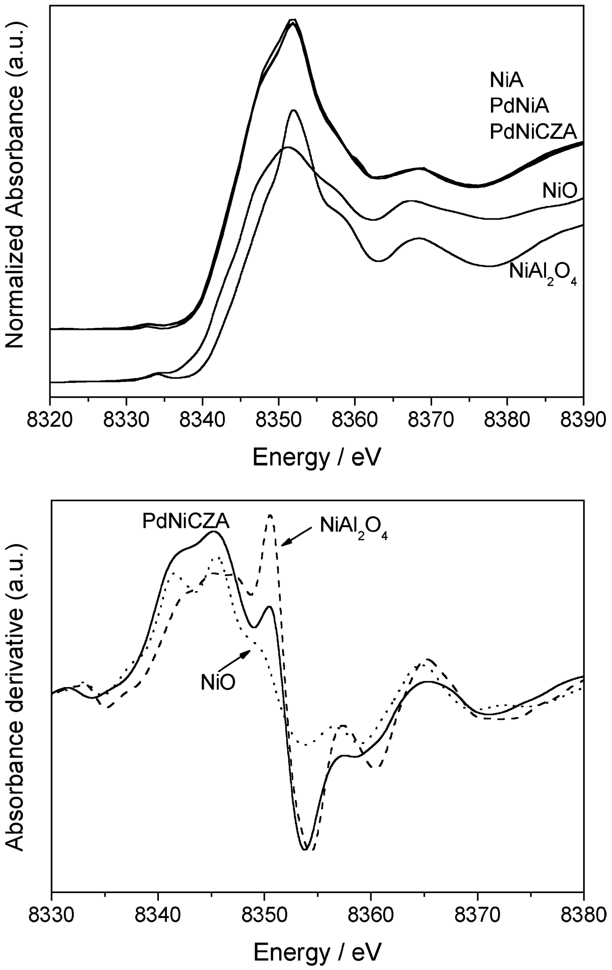

Fig. 6. XANES spectra of NiA, PdNiA, and PdNiCZA samples, and of NiO and $NiAl_2O_4$ references (top). First derivative spectra of the references compared with that of PdNiCZA (bottom).

Ni-containing particles in the Z-contrast images depends essentially on atomic number differences between these and elemental components of the support. In this respect, working with the samples containing CZ can be more difficult. Nevertheless, information on such particles can be derived through analysis of characteristic peaks in the EELS spectra recorded for multiple points of the sample, although interpretation of these spectra in samples with a relatively heterogeneous composition, like those examined here, can be complicated.

Fig. 7 shows a typical Z-contrast image of PdNiA. In all cases, images obtained for this catalyst show numerous small particles exhibiting a stronger contrast than the support and thus related to the presence of the metallic component. This finding is confirmed by analysis of the EELS spectra in which peaks due to palladium are apparent (Fig. 7). Determination of the chemical state of palladium is complicated by interference with the oxygen K-edge, although some of the particles that appear in profile view could be identified as metallic palladium particles (Fig. 7). It should be noted that such a metallic state must be a consequence of palladium reduction under the electron beam, because XANES spectra reveal the presence of essentially PdO-type particles for the initial calcined system [12]. Of note, it was not possible to identify the presence of nickel in any of the multiple spectra analyzed. Even considering that the EELS cross-section of nickel is small compared with that of palladium, the absence of hints of this element in all of the EELS spectra recorded is a strong indication of its high dispersion degree, in agreement with XPS results (Table 2). This is in line with the reported difficulties in identifying highly dispersed particles of copper in Cu/Al_2O_3 catalysts even after a reduction treatment under H_2 at 573 K [37]. The absence of features attributable to the presence of nickel is common to the three Pd–Ni catalysts analyzed in this work (PdNiA, PdNiCZA, and PdNiCZ).

In a similar study performed for PdNiCZA, direct identification of Pd-containing particles in the Z-contrast images was generally more difficult than for PdNiA as a consequence of the smaller atomic number differences with the support constituents. Preferential interaction of palladium with CZ (Fig. 4) further complicates this analysis. Fig. 8 shows a selected case in which palladium particles in zones where CZ and alumina are present could be identified according to information achieved from the EELS spectra. However, in the general case, identifying palladium particles in contact with CZ is quite difficult. To demonstrate this, several analyses using the so-called "line-profile" mode were carried out in zones where low con-

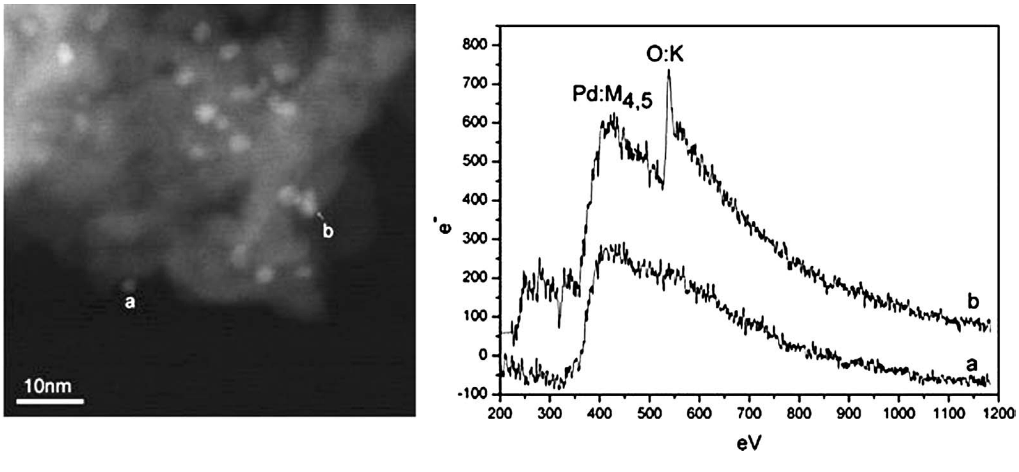

Fig. 7. Z-Contrast image of PdNiA (left) and EELS spectra taken at zones marked in the image (right).

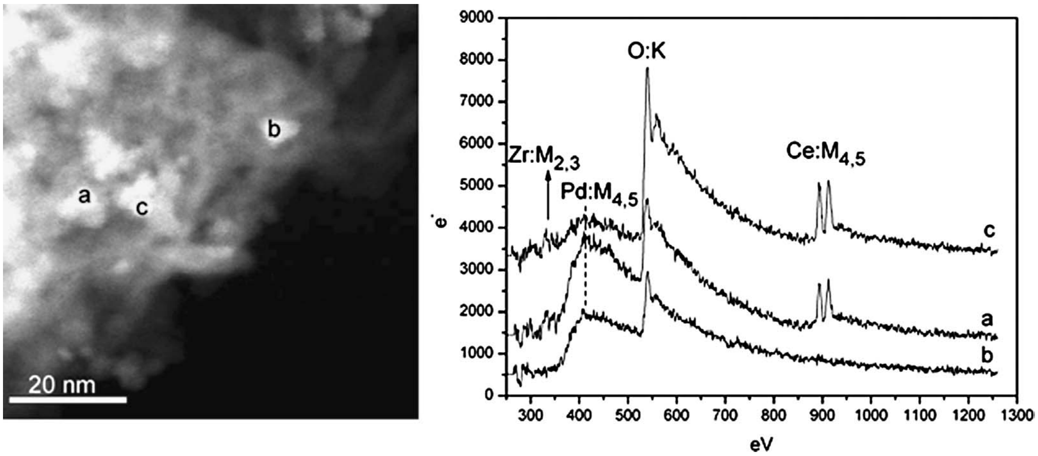

Fig. 8. Z-Contrast image of PdNiCZA (left) and EELS spectra taken at zones marked in the image (right).

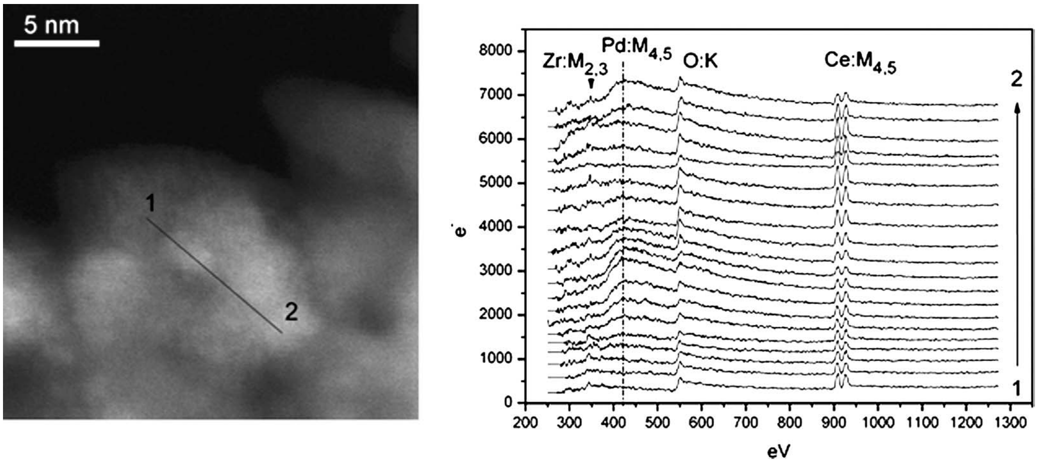

Fig. 9. Z-Contrast image of PdNiCZA (left). EELS spectra taken every ca. 6 Å along the line marked in the image (right).

trast differences do not allow unambiguous identification of palladium particles. This method involves recording a series of EELS spectra along an imaginary line traced over the Z-contrast image. Fig. 9 shows a characteristic example in which 18 EELS spectra were recorded along a ca. 11-nm line (i.e., one spectrum every ca. 6 Å). Analysis of those spectra reveals the existence of at least two different palladium particles in contact with CZ along the analyzed line. Of note, in contrast to results obtained for PdNiCZ (which apparently displays very high palladium dispersion, as discussed later), relatively large particle sizes (around 2 nm) are inferred from the EELS spectra for these palladium particles.

For the PdNiCZ system, identification of palladium particles on the basis of simple examination of contrast differences in the Z-contrast images becomes impossible. Furthermore, it is noteworthy that analysis of 50 EELS spectra in different zones of the sample failed to reveal Pd-related peaks (even using the first derivative registration mode, which in principle allows more facile detection of possible absorption edges). Fig. 10 shows a typical example of this situation. This suggests, as pointed out earlier for nickel, that palladium can have a higher dispersion state in this catalyst. In accordance with this hypothesis, higher dispersion states of palladium and other noble metals have been reported to occur on its dispersion over ceria with respect to alumina supports [38,39]. To corroborate this hypothesis, EXAFS spectra at the Pd K-edge were analyzed for the Pd–Ni catalysts. The Fourier transforms of PdNiCZ and PdNiA (Fig. 11) show the presence of a Pd–O first coordination shell and two contributions corresponding to two Pd–Pd distances (between ca. 3.04 and 3.42 Å), all of which are characteristic of the PdO structure (JCPDS 85-0713). Apart from small differences in the first Pd–O coordination shell, Fig. 11 gives evidence of the almost full lack of the Pd^{2+}–Pd^{2+} coordination shell at ca. 3.1 Å for PdNiA, whereas a bulk-like intensity can be observed for PdNiA. This means that a notable reduction in the number of neighbors at cation–cation first distance was detected for the PdO particles supported on CZ with respect to the PdO bulk reference, whereas no difference was detected for those particles supported on alumina. This gives qualitative support to the foregoing argument concerning Pd dispersion throughout the series of catalysts.

XEDS/EELS studies similar to those done for the corresponding Pd–Ni catalysts were carried out for the monometallic PdA and PdCZA systems to analyze the possible effects of nickel presence on the Pd–Ni system. The main difference was observed for the CZA-supported system, in which

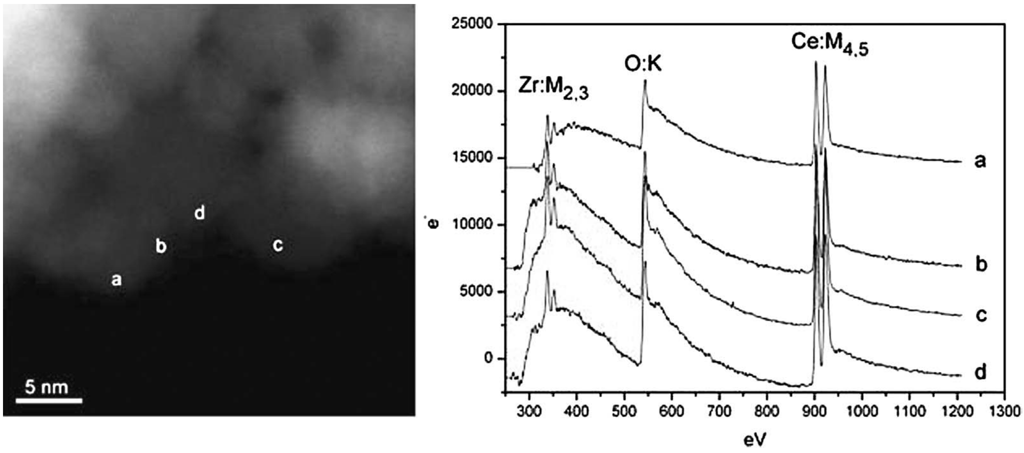

Fig. 10. Z-Contrast image of PdNiCZ (left). EELS spectra taken at the zones marked in the image (right).

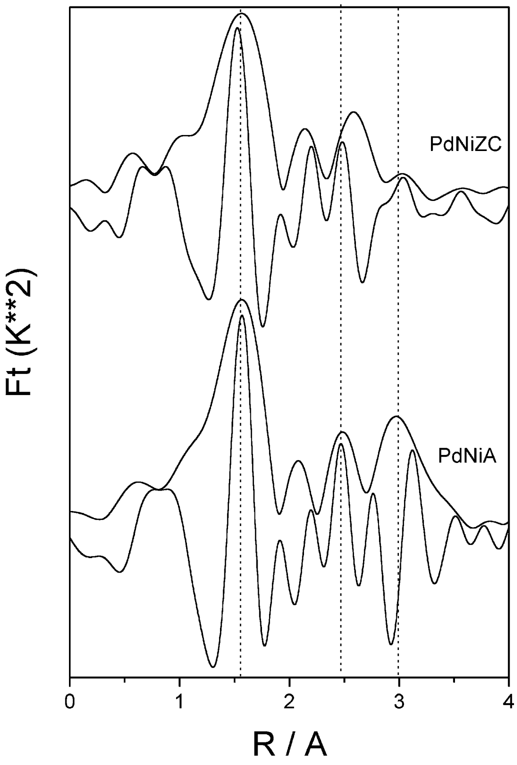

Fig. 11. Fourier transforms of EXAFS spectra in the Pd K-edge for the indicated samples.

detection of palladium particles on direct analysis of the Z-contrast images became more frequent for the monometallic system. This indicates that the presence of nickel forces palladium toward a preferential interaction with CZ in the Pd–Ni catalyst, in agreement with XEDS results of Fig. 4. On the other hand, as has been shown elsewhere [40], analysis of the Z-contrast images allowed extraction of particle size distribution diagrams. Fig. 12 shows such diagrams for the A- and CZA-supported catalysts. These must both be essentially related to the palladium particles in contact with the alumina component of the catalyst (as explained earlier, regions rich in Ce–Zr oxide are not useful for this analysis).

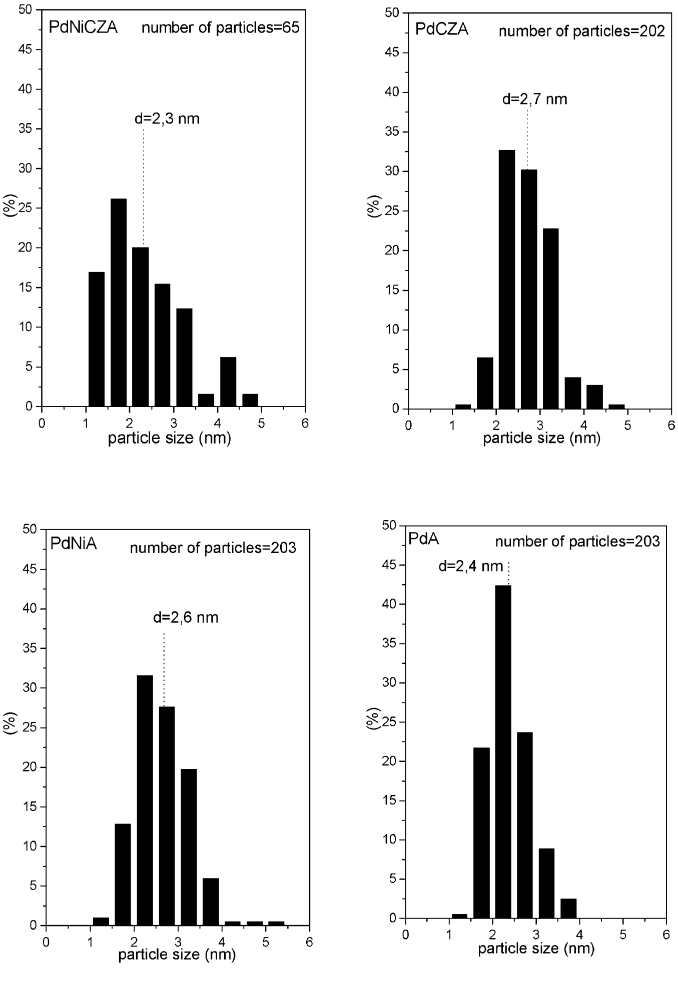

Fig. 12. Particle size distribution histograms extracted from Z-contrast images for the indicated samples. Vertical lines mark average diameters calculated.

4. Summary and conclusions

Morphologic/structural characterization at a nanoscopic level of Pd–Ni catalysts supported on alumina (PdNiA), Ce–Zr mixed oxide/alumina (PdNiCZA), and Ce–Zr mixed oxide (PdNiCZ) has been achieved using primarily electron microscopy-related techniques (i.e., HREM, XEDS, and STEM-EELS). HREM analysis of the support materials, prepared using a microemulsion method, complements previous investigations done by XRD, TEM/XEDS, and Raman [20,21]. The presence of rather homogeneous Ce–Zr mixed-oxide nanostructures (average particle size of 3.4 for CZA and 5.4 nm for CZ) with relatively low dispersion in particle size distribution was seen. Nanoprobe XEDS analysis of the PdNiCZA catalyst revealed a particular trend toward the interaction of palladium and the Ce–Zr mixed-oxide component of the support, enhanced by the presence of nickel in the catalyst, also in agreement with results obtained by STEM-HAADF. Alternatively, nickel appeared to interact preferentially with the alumina component of the support on the basis of such XEDS results. This finding was confirmed by FMR experiments. The chemical nature of the palladium and nickel components of the catalysts was explored with XPS and XANES experiments (see also part 2 of this work [12]). The results demonstrate that palladium appears in the form of small PdO-type particles [12], whereas nickel appears to form small NiO-type particles as well as, for alumina-supported samples, $NiAl_2O_4$-type particles. Overall, the results suggest that no strong interactions between Pd and Ni are present in the initial calcined systems. The dispersion of Pd and the corresponding characteristic size of the PdO particles are strongly influenced by the support nature, being similar for systems having alumina as the carrier and much smaller for those supported on CZ. Finally, analyses of Z-contrast images and EELS spectra done with a STEM instrument confirm the trends observed by XEDS with respect to distributions of the metals over the support (with respect to the existence of preferential interactions with specific support components) in PdNiCZA. Even though direct observation of the Z-contrast images of palladium particles is difficult when the Ce–Zr mixed oxide is present in the catalysts, simultaneous recording of EELS spectra indicates the presence of contacts between both components, in which palladium particles could present a relatively large particle size compared to those present in PdNiCZ. These STEM/EELS and XPS experiments suggest a high degree of nickel dispersion for the three Pd–Ni catalysts, whereas palladium appears to be most dispersed for the PdNiCZ system (as also confirmed by EXAFS analysis). Particle size distributions of palladium are determined from direct analysis of the Z-contrast images in A- or CZA-supported systems (for the latter, related mainly to palladium particles in alumina-enriched zones), demonstrating average sizes of about 2.5 nm, fairly independent of the presence of nickel in the catalyst.

Acknowledgments

The authors thank the scientific and technical staff at Station 9.3 of the SRS synchrotron (Drs. A.R. Lennie and I. Harvey) and Dr. A. Iglesias-Juez of the ICP-CSIC for their help in recording the XAFS spectra (under award No 40115). They also thank F. Sánchez Constenla and E. Pardo for recording the FMR and XPS spectra, respectively. A.B.H. thanks the Comunidad de Madrid for a doctoral studies grant and for financial support through the “Ayudas para estancias en centros extranjeros” program. Support for this work was also provided by the CICyT (project MAT2000-1467), the Office of Science of the U.S. Department of Energy (contract DE-AC03-76SF00098), and the Petroleum Research Fund (contract 37552-AC5).

References

[1] E.S.J. Lox, B.H. Engler, in: G. Ertl, H. Knözinger, J. Weitkamp (Eds.), Environmental Catalysis, Wiley–VCH, 1999, p. 1.
[2] A. Martínez-Arias, J.C. Conesa, M. Fernández-García, J.A. Anderson, in: J.A. Anderson, M. Fernández-García (Eds.), Supported Metals in Catalysis, Imperial College Press, 2005, p. 283.
[3] J. Kašpar, P. Fornasiero, in: A. Trovarelli (Ed.), Catalysis by Ceria and Related Materials, Imperial College Press, 2002, p. 217.
[4] R. van Yperen, D. Lindner, L. Mubmann, E.S. Lox, T. Kreuzer, Stud. Surf. Sci. Catal. 116 (1998) 51.
[5] J.F. Trillat, J. Massadier, B. Morawek, H. Praliaud, A.J. Renouprez, Stud. Surf. Sci. Catal. 116 (1998) 103.
[6] A. El Hamdaoui, G. Bergeret, J. Massadier, M. Primet, A.J. Renouprez, J. Catal. 148 (1994) 47.
[7] M. Fernández-García, A. Martínez-Arias, C. Belver, J.A. Anderson, J.C. Conesa, J. Soria, J. Catal. 190 (2000) 387.
[8] A.B. Hungría, A. Iglesias-Juez, A. Martínez-Arias, M. Fernández-García, J.A. Anderson, J.C. Conesa, J. Soria, J. Catal. 206 (2002) 281.
[9] S. Yamamoto, K. Matsushita, Y. Hanaki, Nipon Kagaku Kaishi (2001) 19.
[10] M. Fernández-García, A. Martínez-Arias, A. Iglesias-Juez, A.B. Hungría, J.A. Anderson, J.C. Conesa, J. Soria, Appl. Catal. B 31 (2001) 39.
[11] A. Martínez-Arias, M. Fernández-García, A. Iglesias-Juez, A.B. Hungría, J.A. Anderson, J.C. Conesa, J. Soria, Appl. Catal. B 31 (2001) 51.
[12] A.B. Hungría, M. Fernández-García, J.A. Anderson, A. Martínez-Arias, J. Catal., in press, Part 2 (this volume), 10.1016/j.cat.2005.08.012.
[13] A. Martínez-Arias, M. Fernández-García, A.B. Hungría, A. Iglesias-Juez, K. Duncan, R. Smith, J.A. Anderson, J.C. Conesa, J. Soria, J. Catal. 204 (2001) 238.
[14] M. Fernández-García, A. Martínez-Arias, A.B. Hungría, A. Iglesias-Juez, J.C. Conesa, J. Soria, Phys. Chem. Chem. Phys. 4 (2002) 2473.
[15] A.B. Hungría, PhD Thesis, Universidad Autónoma de Madrid (2004).
[16] A. Martínez-Arias, M. Fernández-García, V. Ballesteros, L.N. Salamanca, C. Otero, J.C. Conesa, J. Soria, Langmuir 15 (1999) 4796.
[17] P.H. Bolt, F.H.P.M. Habraken, J.W. Geus, J. Catal. 151 (1995) 300.
[18] C.D. Wagner, L.E. Davis, M.V. Teller, J.A. Taylor, R.M. Raymond, L.H. Gale, Surf. Interface Anal. 3 (1981) 211.
[19] A. Laachir, V. Perrichon, A. Badri, J. Lamotte, E. Catherine, J.C. Lavalley, J. El Fallah, L. Hilaire, F. le Normand, E. Quéméré, G.N. Sauvion, O. Touret, J. Chem. Soc., Faraday Trans. 87 (1991) 1601.
[20] A. Martínez-Arias, M. Fernández-García, A.B. Hungría, J.C. Conesa, G. Munuera, J. Phys. Chem. B 107 (2003) 2667.
[21] M. Fernández-García, A. Martínez-Arias, A. Iglesias-Juez, C. Belver, A.B. Hungría, J.C. Conesa, J. Soria, J. Catal. 194 (2000) 385.
[22] M. Yashima, H. Arashi, M. Kakihana, M. Yoshimura, J. Am. Ceram. Soc. 77 (1994) 1067.
[23] M. Fernández-García, A. Martínez-Arias, J.C. Hanson, J.A. Rodríguez, Chem. Rev. 104 (2004) 4063.
[24] R. Di Monte, J. Kaŝpar, J. Mater. Chem. 15 (2005) 633.
[25] A. Martínez-Arias, M. Fernández-García, A.B. Hungría, J.C. Conesa, J. Soria, J. Alloys Compd. 323–324 (2001) 605.
[26] A. Martínez-Arias, M. Fernández-García, L.N. Salamanca, R.X. Valenzuela, J.C. Conesa, J. Soria, J. Phys. Chem. B 104 (2000) 4038.
[27] S. Tsunekawa, S. Ito, Y. Kawazoe, J.-T. Wang, Nano Lett. 3 (2003) 871.
[28] R.J. Matyi, L.H. Schwartz, J.B. Butt, Catal. Rev. Sci. Eng. 29 (1987) 41.
[29] L. Bonneviot, M. Che, D. Olivier, G.A. Martin, E. Freund, J. Phys. Chem. 90 (1986) 2112.
[30] S. Wang, G.C. Max Lu, Appl. Catal. B 19 (1998) 267.
[31] J.A. Montoya, E. Romero-Pascual, C. Gimon, P. Del Angel, A. Monzón, Catal. Today 63 (2000) 71.
[32] S. Yamamoto, K. Matsushita, Nipon Kagaku Kaishi (2000) 553.

[33] S. Uhlenbrock, C. Scharfschwerdt, M. Neumann, G. Illing, H.-J. Freund, J. Phys. Condens. Matter 4 (1992) 7973.
[34] L. Salvati, L.E. Makovsky, J.M. Stencel, F.R. Brown, D.M. Hercules, J. Phys. Chem. 85 (1981) 3700.
[35] J.A. Schreifels, P.C. Maybury, W.E. Swartz, J. Catal. 65 (1980) 195.
[36] N.D. Browning, D.J. Wallis, P.D. Nellist, S.J. Pennycook, Micron 28 (1997) 333.
[37] K. Sun, J. Liu, N.D. Browning, Appl. Catal. B 38 (2002) 271.
[38] S. Bernal, J.J. Calvino, J.M. Gatica, C. López Cartes, J.M. Pintado, in: A. Trovarelli (Ed.), Catalysis by Ceria and Related Compounds, Imperial College Press, 2002, p. 85.
[39] A. Trovarelli, Catal. Rev. Sci. Eng. 38 (1996) 97, and references therein.
[40] K. Sun, J. Liu, N.K. Nag, N.D. Browning, J. Phys. Chem. B 106 (2002) 12239.